A mixed-signal analogue front-end for brain-implantable neural interfaces using a digital fixed-point IIR filter and bulk offset cancellation

Dimitris Antoniadis[1,2], Timothy G. Constandinou[1,2,3]
[1]Dept. of Electrical & Electronic Engineering, Imperial College London, South Kensington Campus, London, SW7 2AZ, UK
[2]UK Dementia Research Institute Centre for Care Research & Technology at Imperial College London & University of Surrey
[3]Mint Neurotechnologies Ltd, 125 Wood Street, London, EC2V 7AW, UK
Email: {dimitris.antoniadis20, t.constandinou}@imperial.ac.uk

arXiv:2511.12540v3 [eess.SP] 1 Jul 2026

***Abstract*—Advances in miniaturised implantable neural electronics have paved the way for therapeutic brain–computer interfaces with clinical potential for movement disorders, epilepsy, and broader neurological applications. This paper presents a mixed-signal analogue front end (AFE) designed to record simultaneously both extracellular action potentials (EAPs) and local field potentials (LFPs). The feedforward path integrates a low-noise amplifier (LNA) and a successive-approximation-register (SAR) analogue-to-digital converter (ADC), while the feedback path employs a fixed-point infinite-impulse-response (IIR) Chebyshev Type II low-pass filter to suppress sub-mHz components via bulk-voltage control of the LNA input differential pair using two R–2R pseudo-resistor digital-to-analogue converters (DACs). The proposed AFE employs a low-power (LP) mode and an offset-cancellation high-performance (HP) mode. The proposed AFE achieves 40.55 dB gain and supports neural recording from 0.1 Hz to 5.705 / 9.66 kHz (LP / HP), with typical input-referred noise of 3.9 / 6.615 μV_{rms} in the LFP band and 11.42 / 11.11 μV_{rms} in the EAP band (LP / HP). Its typical power per channel is 5.44 µW (LP) and 11.35 µW (HP), while it occupies 0.198 mm^2.**

I. Introduction

Advances in miniaturised implantable neural electronics have enabled brain-machine interface applications [1]–[5], with growing clinical potential for movement disorders, epilepsy, and broader neurological and bioelectronic-medicine applications [6]–[11]. A key requirement for implantable neural interfaces is detecting extracellular action potentials (EAPs), typically 50 μV_{pp} to 500 μV_{pp} from 100 Hz to 10 kHz [12], [13], and sensing local field potentials (LFPs) of 0.5 mV_{pp} to 5 mV_{pp} across 100 mHz to 200 Hz [14]–[16].

The analogue front end (AFE) of a neural implant handles neural signal acquisition, typically consisting of low-noise amplifiers (LNAs) followed by multiplexing into an analogue-to-digital converter (ADC). Miniaturised electrodes at the tissue interface introduce large, time-varying DC offsets [17]–[19]. AC-coupled AFEs reject these offsets and provide electrical isolation [20], [21], but sub-hertz high-pass behaviour demands prohibitively large coupling capacitors, limiting scalability in high-channel-count systems [20]. One DC-coupled approach achieves offset tolerance through bulk-voltage control via auxiliary analogue circuitry [22], though the high pass corner is implemented using pseudoresistors and capacitors. Mixed-signal techniques including direct digitisation, delta-modulation, switched-capacitor feedback, and input multiplexing have been explored, yet often at the expense of input impedance or increased switching noise [23]–[25]. Recent methods employ digital low-frequency feedback for offset suppression, however the digital filter has been implemented off chip [26]. Another approach implements the digital low pass filtering on chip, achieving better scalability but captures only LFPs [21]. Additionally, a common issue neglected on both DC and AC-coupled neural implants is that one-time post-fabrication digital trimming schemes used for performance configuration are ineffective due to packaging limitations.

This paper presents a mixed-signal DC-coupled AFE for implantable neural recording that combines and enhances previously established offset-cancellation techniques in three ways. First, body potential (BP) referenced biasing is used for all circuits, eliminating reliance on post-fabrication digital trimming to compensate for process-voltage-temperature (PVT) variations — a practical necessity given packaging constraints in implantable systems. Second, building on the principle from [22], electrode DC offset suppression is achieved via bulk-voltage control of the LNA input differential pair, driven by two R–2R pseudo-resistor DACs with a digital servo-path extending the approach from [26]. Third, the required sub-hertz low-pass filtering is realised on-chip using a fixed-point IIR filter in the feedback path — unlike prior work where this is implemented off-chip. An autonomous high-performance (HP) mode is additionally incorporated, activating the offset-cancellation loop upon detection of a significant input offset. The proposed architecture is illustrated in Fig. 1.

Section II details the proposed AFE architecture, Section III reports the simulation results, and Section IV summarises the conclusions and outlines future work.

II. AFE Architecture

A. AFE Architecture Overview

Packaging constraints preclude the use of digital trimming techniques to compensate for PVT variations, necessitating a design approach referenced to a known on-chip potential. A convenient reference is the BP, which can be either sensed or driven depending on the grounding strategy [27]. In this work, BP is set to half the supply voltage and used as the common reference, with all behaviour defined relative to this level.

The system starts at a low-power mode (LP) and the differential neural signal is sensed at the electrode interface around the body potential (BP) common-mode reference.

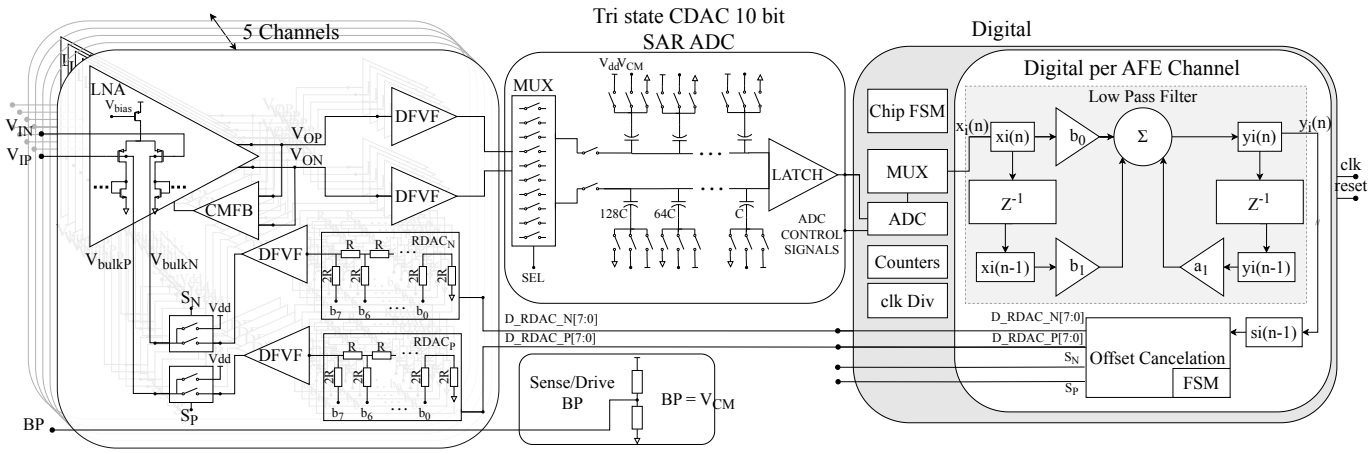

Fig. 1. Architecture of the proposed AFE.

TABLE I
POST LAYOUT LNA PERFORMANCE IN LOW-POWER MODE

Metric	Min	Max	Mean	MC Mean	MC σ
I (µA)	1.37	2.553	1.758	1.672	0.15
f_c (kHz)	3.92	8.26	5.705	5.55	0.61
Gain (dB)	38.26	40.92	39.7	39.66	0.565
Noise_{LF} (μV_{rms})	3.593	4.233	3.904	3.91	0.064
Noise_{HF} (μV_{rms})	9.786	13	11.42	11.47	0.416

Noise_{LF}: 0.1–200 Hz. Noise_{HF}: 200 Hz–10 kHz.

TABLE II
POST LAYOUT LNA PERFORMANCE IN OFFSET-CANCELLATION MODE

Metric	Min	Max	Mean	MC Mean	MC σ
I (µA)	5.253	8.71	6.69	6.571	0.503
f_c (kHz)	7.245	12.97	9.66	9.427	1.408
Gain (dB)	39.46	41.4	40.55	40.39	0.685
Noise_{LF} (μV_{rms})	6.431	6.834	6.615	6.619	0.351
Noise_{HF} (μV_{rms})	9.42	12.76	11.11	11.15	0.37

Noise_{LF}: 0.1–200 Hz. Noise_{HF}: 200 Hz–10 kHz.

The signal is amplified by the low-noise amplifier (LNA) and buffered using two differential flipped-voltage followers (DFVFs). The buffered signal is then multiplexed to a successive-approximation-register (SAR) analogue-to-digital converter (ADC) incorporating a tri-level capacitive DAC (CDAC) [28]. This enables the CDAC conversion to operate around the BP common-mode level. The digitised output is passed through a Chebyshev Type II sub-hertz low-pass filter, which extracts the low-frequency offset component used for digital offset-cancellation control. When this component exceeds a predefined threshold, the high-performance (HP) mode is activated, engaging the offset-cancellation loop. The bulk voltage of the LNA input differential pair is now driven by the outputs of two R–2R DACs, while the LNA bias current is increased to reduce input-referred noise. At reset both DACs are set to maximum code. On detecting a positive offset, RDAC_P decrements, increasing current through the corresponding PMOS device, until the extracted low-frequency component re-enters the target range, at which point the loop holds until re-triggered.

The results presented in the following subsections are obtained from simulations across combinations of typical, fast, and slow corners, as well as Monte Carlo (MC) analysis including device process and mismatch variation, evaluated at temperatures of 25, 36, and 47°C. While body temperature is around 36°C, the two additional temperatures are used to stress the robustness of the devices.

B. Low Noise Amplifier

The technology supports a 1.2 V power supply, so a conventional fully differential current mirror LNA topology was selected to maximise the available dynamic range. With the BP set at half the supply voltage, the differential input pair always operates at an appropriate DC bias level. The common-mode feedback (CMFB) amplifier reference voltage is also set to BP, ensuring proper biasing throughout the signal path. Tab. I and Tab. II report LP and HP performance when driving a DFVF and an additional conservative load of 10 mΩ and 300 fF. The increased HP current arises from driving the LNA bulk terminals through the DFVF output devices. Because the g_{mb} of the input PMOS transistors is lower than their g_m, noise at the DFVF output has significant impact when referred to the LNA input. To reduce this noise to acceptable levels, the LNA bias current is increased during offset cancellation. Analysis showed that 1 mV of input offset can be compensated by applying approximately 2.56 mV to the bulk terminals of the differential input pair. This relationship remains approximately linear over the intended offset-cancellation range.

C. Differential Flipped Voltage Follower

Two variants of a pseudo-differential flipped-voltage follower (DFVF) buffer are employed, chosen for their low power consumption and push–pull output stage, enabling wide bandwidth [29]. The LNA output is buffered using two DFVFs to drive the multiplexer and SAR ADC CDAC (≈30 pF). Additionally, the outputs of the R–2R DACs are buffered using ultra-low-power DFVFs, where the offset-cancellation loop handles only sub-hertz components, reducing bandwidth and current requirements. The performance of the high-bandwidth DFVF driving a conservative 60 pF load is summarised in Tab. III and the low-current DFVF when driving 5 pF is shown in Tab. IV. A positive input offset limits buffer accuracy but is negligible due to its symmetric appearance in the fully differential path.

TABLE III
POST LAYOUT PERFORMANCE OF DFVF BUFFER AT LNA OUTPUT

Metric	Min	Max	Mean	MC Mean	MC σ
I (µA)	0.635	0.907	0.747	0.747	0.07
GBW (kHz)	316.9	429.6	366.5	364.1	44.46
Loop Phase Margin (°)	53.33	62.45	57.97	57.32	3.42
Error (mV)	3.944	8.93	5.77	5.62	4.18

TABLE IV
POST LAYOUT PERFORMANCE OF DFVF AT RDAC OUTPUT

Metric	Min	Max	Mean	MC Mean	MC σ
I (µA)	0.132	0.222	0.158	0.151	0.034
GBW (kHz)	145.2	211	198	204	14.3
Loop Phase Margin (°)	36.2	39.1	37.8	36.5	0.63
Error (mV)	5.67	7.1	6.34	6.27	0.86

D. Resistor DAC

In order to avoid excessive area, the 8-bit R–2R DAC in this design uses pseudo-resistors. Each R unit comprises four pseudo-resistors in series. Across all corners, the effective resistance of R unit ranges from 27.82 TΩ to 136 TΩ. The R unit is also sensitive to RDAC code changes. During code sweep, it exhibits an average step size of 266 µV, with a minimum of 170 µV and a maximum of 2.96 mV at specific transition codes over PVT. This allows the offset-cancellation algorithm to typically reduce the residual offset to around 100 µV, with a worst-case code residual of approximately 1.15 mV. In MC simulation, it exhibits mean step value of 262.5 µV ($\sigma = 6.83$ µV). The MC mean of max step during code sweep is 2.298 mV ($\sigma = 490$ µV). It always remains monotonic. Worst case code residual does not saturate the dynamic input range of the LNA and the offset can later be removed in digital post processing. The RDAC output range spans from 750 mV to 899 mV, ensuring the bulks of the differential pair never become forward-biased. Depending on the code, the current consumption ranges from 1 nA to 150 nA and for MC from 2.5 nA to 91.8 nA (MC mean = 13.78 nA, $\sigma = 14.83$ nA).

E. Tri-state CDAC SAR ADC

The ADC is shared across multiple channels. The chosen architecture is based on the 10-bit differential SAR ADC described in [28], which employs top-plate sampling on the capacitive DAC (CDAC). The MSB is set by the first comparison and the remaining bits are resolved by binary search, with the losing side referenced to V_{cm} = BP. Conversion thus remains centred on the BP level. Operating around V_{cm}, the zero-offset reference of the low-pass filter, ensures consistent behaviour across the signal chain and inherent common-mode rejection. The ADC draws 4.12 µA per conversion on average, with 3.64 and 6.27 µA min and max respectively. The 9.3 µs conversion time yields a 107 kHz maximum rate, sufficient to sample five channels at 20 kHz for signals below 10 kHz. The digital power consumption for ADC SAR controller is estimated equal to 2.748 µW from final gds implementation netlist.

F. Digital Low Pass Filter

The digital filter in the feedback path must be as compact and power-efficient as possible. To meet these constraints, an IIR architecture was selected, enabling a low-order implementation with reduced hardware complexity. To minimise area, a fixed-point design was adopted with the smallest coefficient and data word lengths that maintain accuracy. The filter uses a single biquad section—the basic second-order IIR building block—in a Direct Form I structure for reduced hardware and improved overflow handling. A Chebyshev Type II low-pass filter was designed with a 16 kHz sampling frequency, 1 mHz passband edge, 0.1 Hz stopband edge, 0.01 dB passband ripple, and 50 dB stopband attenuation. Fixed-point precision was determined using an adapted methodology from [30], evaluating the L1-norm difference between the ideal double-precision and fixed-point impulse responses over 2^{21} samples. The filter output requires 11 integer bits, and a "sweet spot" of 40 fractional bits was identified where the quantisation error approaches zero, with internal word widths sized accordingly. The digital power consumption is estimated equal to 230 nW from final gds implementation netlist.

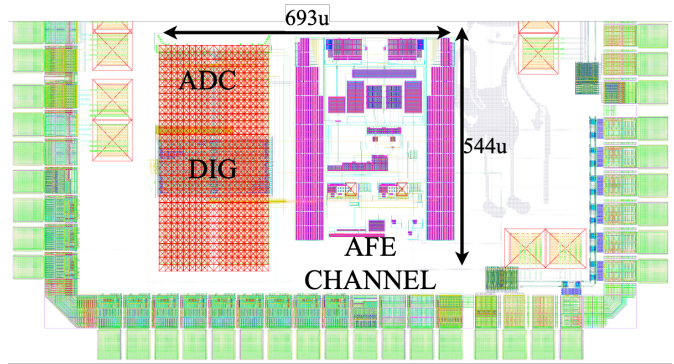

Fig. 2. AFE Layout.

III. RESULTS

The layout shown in Fig. 2, being fabricated in 65 nm CMOS, occupies 693 µm × 544 µm total: 467 µm × 376 µm (0.17 mm^2) for the LNA with buffers and 544 µm × 258 µm (0.14 mm^2) for the ADC. As the ADC area is mostly capacitors, the underlying region remains available for digital logic.

Fig. 4 demonstrates the offset-cancellation mechanism for a 50 Hz, 1 mV input with 1 mV DC offset, with the LNA output sampled at 19.53 kHz. As shown in Fig. 4(a), once HP mode is enabled the RDAC_P code decrements and the LNA output settles around the BP common-mode level, while the SAR code converges to mid-code 512 as depicted in Fig. 4(d). The total current consumption per channel with digital included is typically 4.534 µA (LP) and 9.46 µA (HP). Based on the dynamic range of the RDAC, the system can suppress low-frequency offset components up to ±58.13 mV. The offset-cancellation loop typically reduces the residual offset to ≈100 µV (worst-case 1.15 mV), a quasi-static DC term that does not interfere with detection and is removable in digital post-processing. The typical LNA linear input range is 16.8 mV$_{pp}$ (4.8 mV$_{pp}$ worst-case) at 10 % gain deviation. The channel therefore keeps recording throughout cancellation, at full fidelity when the offset is within range and with increasing distortion for larger initial offsets.

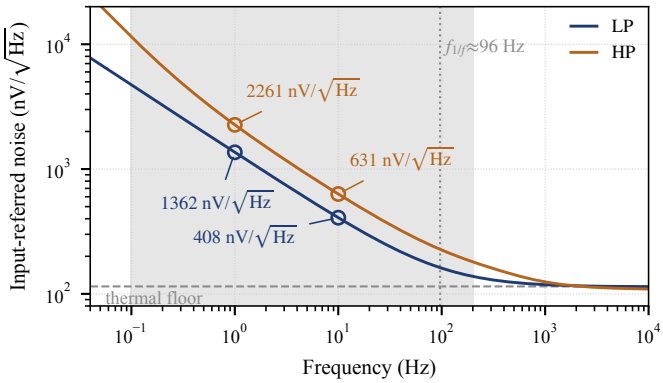

Fig. 3. Input-referred noise PSD in LP and HP modes (typical corner). The shaded region marks the 0.1 – 200 Hz LFP integration band. The 1/f corner lies at ≈ 96 / 334 Hz (LP / HP), above which the thermal floor (≈ 115 nV/$\sqrt{\text{Hz}}$) dominates. Spot values are annotated at 1 Hz and 10 Hz.

A performance comparison with recent state-of-the-art AFEs, for both typical case LP and HP offset-cancellation modes, is provided in Tab. V. The proposed implementation achieves relatively good current and power consumption with digital included for an increased footprint, while HP mode trades noise and efficiency for offset-rejection performance. At LP the proposed implementation does not cover the whole 10 kHz range indicating further improvements could be explored. Its NEF and PEF is higher than the compared works, as expected due to its higher noise. HP mode incurs the expected penalty of the additional RDAC and DFVF bulk-driven path, with PEF rising to 282.3, reflecting the $g_{mb} < g_m$ penalty. The larger area footprint is a consequence of using long-channel devices to maintain current mirror saturation and robustness across PVT. The ADC input-referred LSB of ≈ 12 µV is comparable to the LNA noise floor, suggesting moderate noise-power trade-offs remain available for improvement in future iterations. Fig. 3 shows the typical input-referred noise power spectral density (PSD). The $1/f$ corner is ≈ 96 / 334 Hz (LP / HP), with spot values 1362 nV/$\sqrt{\text{Hz}}$ (LP) at 1 Hz and 631 nV/$\sqrt{\text{Hz}}$ (HP) at 10 Hz. Finally, a limitation is the long settling time of the sub-blocks, imposed by the sub-hertz feedback filter. The chip startup settling is set at 525 s for worst case, the initial RDAC settling can reach 200 s, and ≈ 33 s are required after each 1-bit RDAC update before the next. During the offset cancellation state, larger offsets reduce LNA linearity until partially rejected and brought within range.

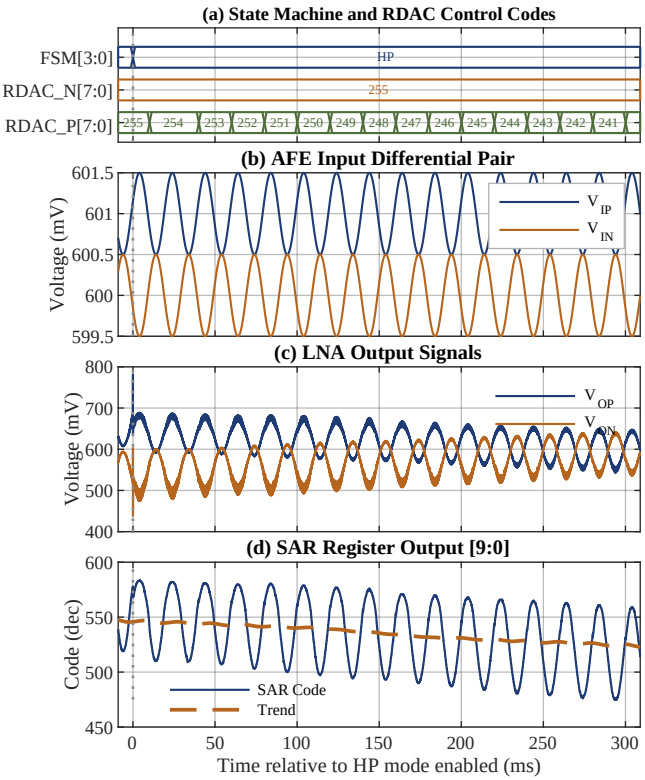

Fig. 4. AFE operation with a 1 mV, 50 Hz differential input and 1 mV DC electrode offset, demonstrating the offset cancellation mechanism converging around mid code 512. For demonstration purposes a faster prescaler clock has been applied at RDAC transitions.

IV. Conclusion

A PVT-tolerant low-power mixed-signal AFE with autonomous DC offset cancellation has been presented, integrating an on-chip fixed-point IIR filter and bulk-voltage control of the LNA input pair. It achieves 40.55 dB gain, 3.9 μV_{rms} typical LFP-band noise and 11.11 μV_{rms} typical EAP-band noise. Finally, it achieves ±58.13 mV offset rejection across the bandwidth of operation, suited to scalable multi-channel implants.

TABLE V
Performance Comparison of Neural Recording AFEs

Metric	[26]	[22]	[31]	[32]	Typical This work†
Technology (nm)	65	180	180	65	65
Supply (V)	0.5	1.8	1.8	1.2/0.8	1.2
Power/ch (µW)	5.04	12.8	14.94	5.8	5.44* (LP), 11.35* (HP)
Area/ch (mm^2)	0.013	0.020	0.480	0.075	0.198
Bandwidth (kHz)	10	10	10	1	5.705 (LP), 9.66 (HP)
Peak input (mV$_{pp}$)	–	19	14	400	16.8‡
EDO range (mV)	±20	±100	±60	±200	±58.125
LFP noise (µV$_{rms}$)	4.3 @ 10–300 Hz	1.82 @ 1–200 Hz	2.72 @ 0.5–1000 Hz	3.5 @ 1–1000 Hz	3.904 (LP), 6.615 (HP) @ 0.1–200 Hz
EAP noise (µV$_{rms}$)	4.9 @ 0.3–10kHz Hz	5.55 @ 0.2–10 kHz	4.37 @ 0.3–10 kHz	–	11.42 (LP), 11.11 (HP) @ 0.2–10 kHz
NEF	5.99	5.75	5.01	–	9.91 (LP), 15.33 (HP)
PEF	17.96	59.5	45	–	117.8 (LP), 282.3 (HP)

EDO: electrode DC-offset cancellation range. LP/HP: low-power / offset-cancellation modes for this work. ‡At 10 % gain deviation.
†This work presents simulation results, while [26], [22], [31], [32] are silicon measured. *Total digital power consumption per channel included.

REFERENCES

[1] A. B. Rapeaux and T. G. Constandinou, "Implantable brain machine interfaces: first-in-human studies, technology challenges and trends," *Current opinion in biotechnology*, vol. 72, pp. 102–111, 2021, [Online].

[2] N. Ahmadi, M. L. Cavuto, P. Feng, L. B. Leene, M. Maslik, F. Mazza, O. Savolainen, K. M. Szostak, C.-S. Bouganis, J. Ekanayake *et al.*, "Towards a distributed, chronically-implantable neural interface," in *2019 9th International IEEE/EMBS Conference on Neural Engineering (NER)*. IEEE, 2019, pp. 719–724, [Online].

[3] R. Muller, M. M. Ghanbari, and A. Zhou, "Miniaturized Wireless Neural Interfaces: A tutorial," *IEEE Solid-State Circuits Magazine*, vol. 13, no. 4, pp. 88–97, 2021, [Online].

[4] K. M. Szostak, P. Feng, F. Mazza, and T. G. Constandinou, *Distributed Neural Interfaces: Challenges and Trends in Scaling Implantable Technology*. Singapore: Springer Singapore, 2020, pp. 1–37, [Online].

[5] E. Musk *et al.*, "An integrated brain-machine interface platform with thousands of channels," *Journal of medical Internet research*, vol. 21, no. 10, p. e16194, 2019, [Online].

[6] J. R. Wolpaw, J. D. R. Millán, and N. F. Ramsey, "Brain-computer interfaces: Definitions and principles," *Handbook of clinical neurology*, vol. 168, pp. 15–23, 2020, [Online].

[7] C. Brunner, N. Birbaumer, B. Blankertz, C. Guger, A. Kübler, D. Mattia, J. d. R. Millán, F. Miralles, A. Nijholt, E. Opisso *et al.*, "BNCI Horizon 2020: towards a roadmap for the BCI community," *Brain-computer interfaces*, vol. 2, no. 1, pp. 1–10, 2015, [Online].

[8] D. J. McFarland, D. J. Krusienski, W. A. Sarnacki, and J. R. Wolpaw, "Emulation of computer mouse control with a noninvasive brain–computer interface," *Journal of neural engineering*, vol. 5, no. 2, p. 101, 2008, [Online].

[9] N. Robinson, R. Mane, T. Chouhan, and C. Guan, "Emerging trends in BCI-robotics for motor control and rehabilitation," *Current Opinion in Biomedical Engineering*, vol. 20, p. 100354, 2021, [Online].

[10] M. A. González-González, S. V. Conde, R. Latorre, S. C. Thébault, M. Pratelli, N. C. Spitzer, A. Verkhratsky, M.-É. Tremblay, C. G. Akcora, A. G. Hernández-Reynoso, M. Ecker, J. Coates, K. L. Vincent, and B. Ma, "Bioelectronic Medicine: a multidisciplinary roadmap from biophysics to precision therapies," *Frontiers in Integrative Neuroscience*, vol. 18, p. 1321872, 2024, [Online].

[11] I. Lerman, Y. Bu, R. Singh, H. A. Silverman, A. Bhardwaj, A. J. Mann, A. Widge, J. Palin, C. Puleo, and H. Lim, "Next generation bioelectronic medicine: making the case for non-invasive closed-loop autonomic neuromodulation," *Bioelectronic Medicine*, vol. 11, no. 1, p. 1, 2025, [Online].

[12] E. R. Kandel, J. H. Schwartz, T. M. Jessell, S. Siegelbaum, A. J. Hudspeth, S. Mack *et al.*, *Principles of neural science*. McGraw-hill New York, 2000, vol. 4.

[13] M. Mollazadeh, K. Murari, G. Cauwenberghs, and N. Thakor, "Wireless micropower instrumentation for multimodal acquisition of electrical and chemical neural activity," *IEEE transactions on biomedical circuits and systems*, vol. 3, no. 6, pp. 388–397, 2009, [Online].

[14] B. Gosselin, "Recent advances in neural recording microsystems," *Sensors*, vol. 11, pp. 4572–4597, 2011, [Online].

[15] J. R. White, T. Levy, W. Bishop, and J. D. Beaty, "Real-time decision fusion for multimodal neural prosthetic devices," *PloS one*, vol. 5, no. 3, p. e9493, 2010, [Online].

[16] P. G. Patil and D. A. Turner, "The development of brain-machine interface neuroprosthetic devices," *Neurotherapeutics*, vol. 5, pp. 137–146, 2008, [Online].

[17] K. Woeppel, Q. Yang, and X. T. Cui, "Recent advances in neural electrode–tissue interfaces," *Current opinion in biomedical engineering*, vol. 4, pp. 21–31, 2017, [Online].

[18] J. Villa, J. Cury, L. Kessler, X. Tan, and C.-P. Richter, "Enhancing biocompatibility of the brain-machine interface: A review," *Bioactive Materials*, vol. 42, pp. 531–549, 2024, [Online].

[19] A. Campbell and C. Wu, "Chronically implanted intracranial electrodes: tissue reaction and electrical changes," *Micromachines*, vol. 9, no. 9, p. 430, 2018, [Online].

[20] A. Uran, Y. Leblebici, A. Emami, and V. Cevher, "An AC-coupled wideband neural recording front-end with sub-1 mm 2× fJ/conv-step efficiency and 0.97 NEF," *IEEE Solid-State Circuits Letters*, vol. 3, pp. 258–261, 2020, [Online].

[21] A. Bagheri, M. T. Salam, J. L. P. Velazquez, and R. Genov, "Low-frequency noise and offset rejection in DC-coupled neural amplifiers: A review and digitally-assisted design tutorial," *IEEE transactions on biomedical circuits and systems*, vol. 11, no. 1, pp. 161–176, 2016, [Online].

[22] M. Sporer, S. Reich, J. G. Kauffman, and M. Ortmanns, "A direct digitizing chopped neural recorder using a body-induced offset based DC servo loop," *IEEE Transactions on Biomedical Circuits and Systems*, vol. 16, no. 3, pp. 409–418, 2022, [Online].

[23] H. Kassiri, M. T. Salam, M. R. Pazhouhandeh, N. Soltani, J. L. P. Velazquez, P. Carlen, and R. Genov, "Rail-to-rail-input dual-radio 64-channel closed-loop neurostimulator," *IEEE Journal of Solid-State Circuits*, vol. 52, no. 11, pp. 2793–2810, 2017, [Online].

[24] J. P. Uehlin, W. A. Smith, V. R. Pamula, S. I. Perlmutter, J. C. Rudell, and V. S. Sathe, "A 0.0023 mm2/ch. Delta-Encoded, Time-Division Multiplexed Mixed-Signal ECoG Recording Architecture With Stimulus Artifact Suppression," *IEEE Transactions on Biomedical Circuits and Systems*, vol. 14, no. 2, pp. 319–331, 2020, [Online].

[25] D. De Dorigo, C. Moranz, H. Graf, M. Marx, D. Wendler, B. Shui, A. S. Herbawi, M. Kuhl, P. Ruther, O. Paul *et al.*, "Fully immersible subcortical neural probes with modular architecture and a delta-sigma ADC integrated under each electrode for parallel readout of 144 recording sites," *IEEE Journal of Solid-State Circuits*, vol. 53, no. 11, pp. 3111–3125, 2018, [Online].

[26] R. Muller, S. Gambini, and J. M. Rabaey, "A 0.013 mm2, 5 μW , DC-Coupled Neural Signal Acquisition IC With 0.5 V Supply," *IEEE Journal of Solid-State Circuits*, vol. 47, no. 1, pp. 232–243, 2011, [Online].

[27] D. Haci, Y. Liu, S. S. Ghoreishizadeh, and T. G. Constandinou, "Design considerations for ground referencing in multi-module neural implants," in *2018 IEEE Biomedical Circuits and Systems Conference (BioCAS)*. IEEE, 2018, pp. 1–4, [Online].

[28] C. Yuan and Y. Lam, "Low-energy and area-efficient tri-level switching scheme for SAR ADC," *Electronics letters*, vol. 48, no. 9, pp. 482–483, 2012, [Online].

[29] J. Ramirez-Angulo, S. Gupta, R. G. Carvajal, and A. J. Lopez-Martin, "New improved CMOS class AB buffers based on differential flipped voltage followers," in *2006 IEEE International Symposium on Circuits and Systems*. IEEE, 2006, pp. 4–pp, [Online].

[30] A. Volkova, M. Istoan, F. De Dinechin, and T. Hilaire, "Towards hardware IIR filters computing just right: Direct form I case study," *IEEE Transactions on Computers*, vol. 68, no. 4, pp. 597–608, 2018, [Online].

[31] D. Wendler, D. De Dorigo, M. Amayreh, A. Bleitner, M. Marx, and Y. Manoli, "28.7 A 0.00378 mm 2 scalable neural recording front-end for fully immersible neural probes based on a two-step incremental delta-sigma converter with extended counting and hardware reuse," in *2021 IEEE International Solid-State Circuits Conference (ISSCC)*, vol. 64. IEEE, 2021, pp. 398–400, [Online].

[32] C. Pochet, J. Huang, P. Mercier, and D. A. Hall, "A 174.7-dB FoM, 2 nd-Order VCO-Based ExG-to-Digital Front-End Using a Multi-Phase Gated-Inverted-Ring Oscillator Quantizer," *IEEE Transactions on Biomedical Circuits and Systems*, vol. 15, no. 6, pp. 1283–1294, 2021, [Online].